

# Kinematics-Based Sensor Fault Detection for Autonomous Vehicles Using Real-Time Numerical Differentiation

Shashank Verma\*, Yousaf Rahman, E. Dogan Sumer, and Dennis S. Bernstein\*

**Abstract**—Sensor fault detection is of extreme importance for ensuring the safe operation of vehicles. This paper introduces a novel approach to detecting and identifying faulty sensors. For ground vehicles confined to the horizontal plane, this technique is based on six kinematics-based error metrics that are computed in real time by using onboard sensor data encompassing compass, radar, rate gyro, and accelerometer measurements as well as their derivatives. Real-time numerical differentiation is performed by applying the adaptive input and state estimation (AIE/ASE) algorithm. Numerical examples are provided to assess the efficacy of the proposed methodology.

## I. INTRODUCTION

Greater autonomy for ground vehicles requires a greater number of sensors, and thus more opportunity for sensor failure. This, in turn, leads to a greater need to detect and diagnose sensor faults. Detection and diagnose of sensor failure is thus an important area of research [1], [2].

Sensor fault detection [3] is a subset of fault detection and diagnosis [4]–[17]. In some cases, sensor health can be assessed by exciting the system in a controlled manner, using a plant model and an observer to predict the response, and by comparing the measured response to the prediction. This approach, known as *active* sensor fault detection, is based on *residual generation* [7], [8], [18]–[24]. In contrast, *passive* sensor fault detection detects sensor faults by analyzing each sensor signal separately and searching for anomalies [25]–[31]. Sensor fault detection for aircraft is considered in [32]–[34].

Detecting sensor faults is a challenging problem for several reasons. First, a sensor can fail in numerous ways: gradually, suddenly, or intermittently, with unknown bias, scale factor, and nonlinearity. In addition, it may be difficult to distinguish sensor failure from the effects of disturbances and system changes. The challenging dilemma is that the validity of sensor measurements tends to be most questionable during rare and dangerous events, which is precisely when measurements are most needed to enable corrective action. In order to avoid catastrophe, it is therefore essential to detect the onset of sensor faults and diagnose those faults so that a decision can rapidly be reached as to whether the sensor data are valid.

The contents of the paper are as follows. Section II presents the single and double transport theorem. Section III discusses using sensor data in single and double transport theorem. Section IV describes the adaptive input estimation with adaptive state estimation algorithm. Section V present

the error metrics for the sensor fault detection. Section VI discusses the sensor fault detection for ground vehicle and present a method to identify the fault sensor. Finally, Section VII showcases two examples illustrating sensor fault detection in rate gyro and accelerometer sensors.

## II. PROBLEM FORMULATION

We assume the Earth is inertially nonrotating and nonaccelerating. The right-handed frame  $F_E = [\hat{i}_E \ \hat{j}_E \ \hat{k}_E]$  is fixed to the Earth, and the origin  $o_E$  of  $F_E$  is any convenient point fixed on the Earth; hence,  $o_E$  has zero inertial acceleration.  $\hat{k}_E$  points downward, and  $\hat{i}_E$  and  $\hat{j}_E$  are horizontal. The right-handed vehicle body-fixed frame is denoted by  $F_B = [\hat{i}_B \ \hat{j}_B \ \hat{k}_B]$ . The origin  $o_B$  of  $F_B$  is any point fixed on the vehicle,  $\hat{i}_B$  is pointing forward of the vehicle,  $\hat{j}_B$  is directed out the right side of the vehicle, and  $\hat{k}_B$  is directed downward.

Next,  $F_E$  and  $F_B$  are related by

$$F_B = \vec{R}_{B/E} F_E, \quad (1)$$

where  $\vec{R}_{B/E}$  is the physical rotation matrix

$$\vec{R}_{B/E} = \vec{R}_{\hat{k}_E}(\theta), \quad (2)$$

where

$$\vec{R}_{\hat{k}_E}(\theta) \triangleq (\cos \theta) \vec{I} + (1 - \cos \theta) \hat{k}_E \hat{k}_E' + (\sin \theta) \hat{k}_E^\times, \quad (3)$$

$\vec{I}$  is the physical identity matrix, and the superscript  $\times$  creates a skew-symmetric physical matrix. Note that (3) represents a right-hand-rule rotation about the eigenaxis  $\hat{k}_E$  by the eigenangle  $\theta$ . The physical angular velocity  $\vec{\omega}_{B/E}$  of  $F_B$  relative to  $F_E$  is defined by Poisson's equation

$$\overset{B\bullet}{\vec{R}}_{B/E} = \vec{R}_{B/E} \vec{\omega}_{B/E}^\times, \quad (4)$$

where  $\overset{B\bullet}{\cdot}$  denotes the time derivative with respect to  $F_B$ .

The location of the vehicle center of mass  $o_B$  relative to  $o_E$  at each time instant is given by a physical position vector  $\vec{r}_{o_B/o_E}$ . The first and second derivatives of  $\vec{r}_{o_B/o_E}$  with respect to  $F_E$  are provided by the single and double transport theorems, respectively, which have the forms

$$\overset{E\bullet}{\vec{r}}_{o_B/o_E} = \overset{B\bullet}{\vec{r}}_{o_B/o_E} + \vec{\omega}_{B/E} \times \vec{r}_{o_B/o_E}, \quad (5)$$

$$\overset{E\bullet\bullet}{\vec{r}}_{o_B/o_E} = \overset{B\bullet\bullet}{\vec{r}}_{o_B/o_E} + 2\vec{\omega}_{B/E} \times \overset{B\bullet}{\vec{r}}_{o_B/o_E} + \overset{B\bullet}{\vec{\omega}}_{B/E} \times \vec{r}_{o_B/o_E} + \vec{\omega}_{B/E} \times (\vec{\omega}_{B/E} \times \vec{r}_{o_B/o_E}). \quad (6)$$

\*Shashank Verma and Dennis S. Bernstein are with the Department of Aerospace Engineering, University of Michigan, Ann Arbor, MI 48109, USA shaaero@umich.edu

Note that (5) and (6) are exact kinematic relations.

### III. USING DATA IN SINGLE AND DOUBLE TRANSPORT

The vehicle is equipped with onboard sensors including a compass, radar, rate gyro, and accelerometer. We assume that the azimuth of vehicle may vary with time, but otherwise the vehicle remains horizontal at all times, that is, the elevation and bank angles are always zero. Hence, the eigenangle  $\theta$  is the azimuth angle. To evaluate the terms in (5) and (6) using sensor data, we begin by resolving all the terms on the right-hand side (RHS) of (5) and (6) in  $F_B$ , which yields

$$\begin{bmatrix} r_x \\ r_y \\ r_z \end{bmatrix} \triangleq \vec{r}_{\text{OB/OE}} \Big|_B, \quad \begin{bmatrix} \dot{r}_x \\ \dot{r}_y \\ \dot{r}_z \end{bmatrix} = \overset{B\bullet}{\vec{r}}_{\text{OB/OE}} \Big|_B, \quad (7)$$

$$\begin{bmatrix} \ddot{r}_x \\ \ddot{r}_y \\ \ddot{r}_z \end{bmatrix} = \overset{B\bullet\bullet}{\vec{r}}_{\text{OB/OE}} \Big|_B, \quad (8)$$

$$\begin{bmatrix} \omega_x \\ \omega_y \\ \omega_z \end{bmatrix} \triangleq \vec{\omega}_{B/E} \Big|_B, \quad \begin{bmatrix} \dot{\omega}_x \\ \dot{\omega}_y \\ \dot{\omega}_z \end{bmatrix} = \overset{B\bullet}{\vec{\omega}}_{B/E} \Big|_B. \quad (9)$$

We can resolve (2) in  $F_B$  as

$$\mathcal{O}_{E/B}(\theta) \triangleq \vec{R}_{B/E} \Big|_B = \begin{bmatrix} \cos \theta & -\sin \theta & 0 \\ \sin \theta & \cos \theta & 0 \\ 0 & 0 & 1 \end{bmatrix}, \quad (10)$$

where  $\mathcal{O}_{E/B}(\theta)$  is an orientation matrix.

To resolve the left-hand side (LHS) of (5) in  $F_B$ , we first resolve the position vector  $\vec{r}_{\text{OB/OE}}$  in  $F_E$  to obtain

$$\begin{bmatrix} R_x \\ R_y \\ R_z \end{bmatrix} \triangleq \vec{r}_{\text{OB/OE}} \Big|_E = \mathcal{O}_{E/B}(\theta) \begin{bmatrix} r_x \\ r_y \\ r_z \end{bmatrix}, \quad (11)$$

and then we differentiate once and twice to obtain

$$\begin{bmatrix} \dot{R}_x \\ \dot{R}_y \\ \dot{R}_z \end{bmatrix} = \overset{E\bullet}{\vec{r}}_{\text{OB/OE}} \Big|_E = \frac{d}{dt} \left( \mathcal{O}_{E/B}(\theta) \begin{bmatrix} r_x \\ r_y \\ r_z \end{bmatrix} \right), \quad (12)$$

$$\begin{bmatrix} \ddot{R}_x \\ \ddot{R}_y \\ \ddot{R}_z \end{bmatrix} = \overset{E\bullet\bullet}{\vec{r}}_{\text{OB/OE}} \Big|_E = \frac{d^2}{dt^2} \left( \mathcal{O}_{E/B}(\theta) \begin{bmatrix} r_x \\ r_y \\ r_z \end{bmatrix} \right). \quad (13)$$

Now, define

$$\begin{bmatrix} V_x \\ V_y \\ V_z \end{bmatrix} \triangleq \overset{E\bullet}{\vec{r}}_{\text{OB/OE}} \Big|_B = \mathcal{O}_{B/E}(\theta) \begin{bmatrix} \dot{R}_x \\ \dot{R}_y \\ \dot{R}_z \end{bmatrix}, \quad (14)$$

$$\begin{bmatrix} A_x \\ A_y \\ A_z \end{bmatrix} \triangleq \overset{E\bullet\bullet}{\vec{r}}_{\text{OB/OE}} \Big|_B = \mathcal{O}_{B/E}(\theta) \begin{bmatrix} \ddot{R}_x \\ \ddot{R}_y \\ \ddot{R}_z \end{bmatrix}. \quad (15)$$

Resolving (5) and (6) in  $F_B$ , and rewriting (15) yields

$$\begin{bmatrix} V_x \\ V_y \\ V_z \end{bmatrix} = \begin{bmatrix} \dot{r}_x \\ \dot{r}_y \\ \dot{r}_z \end{bmatrix} + \begin{bmatrix} \omega_x \\ \omega_y \\ \omega_z \end{bmatrix} \times \begin{bmatrix} r_x \\ r_y \\ r_z \end{bmatrix}, \quad (16)$$

$$\begin{bmatrix} A_x \\ A_y \\ A_z \end{bmatrix} = \begin{bmatrix} \ddot{r}_x \\ \ddot{r}_y \\ \ddot{r}_z \end{bmatrix} + 2 \begin{bmatrix} \omega_x \\ \omega_y \\ \omega_z \end{bmatrix} \times \begin{bmatrix} \dot{r}_x \\ \dot{r}_y \\ \dot{r}_z \end{bmatrix} + \begin{bmatrix} \dot{\omega}_x \\ \dot{\omega}_y \\ \dot{\omega}_z \end{bmatrix} \times \begin{bmatrix} r_x \\ r_y \\ r_z \end{bmatrix} + \begin{bmatrix} \omega_x \\ \omega_y \\ \omega_z \end{bmatrix} \times \left( \begin{bmatrix} \omega_x \\ \omega_y \\ \omega_z \end{bmatrix} \times \begin{bmatrix} r_x \\ r_y \\ r_z \end{bmatrix} \right), \quad (17)$$

$$\begin{bmatrix} A_x \\ A_y \\ A_z \end{bmatrix} = \mathcal{O}_{B/E}(\theta) \begin{bmatrix} \ddot{R}_x \\ \ddot{R}_y \\ \ddot{R}_z \end{bmatrix}. \quad (18)$$

Table I enumerates the data available from onboard sensors along with the derivatives that are computed in order to evaluate all of the terms in (16), (17), and (18). To compute these derivatives, we apply the adaptive estimation algorithm described in Section IV.

Sensors	Data	Processed Data
Compass	$\theta$	
Radar	$r_x, r_y, r_z$	$\dot{r}_x, \dot{r}_y, \dot{r}_z,$ $\ddot{r}_x, \ddot{r}_y, \ddot{r}_z$
Rate gyro	$\omega_x, \omega_y, \omega_z$	$\dot{\omega}_x, \dot{\omega}_y, \dot{\omega}_z$
Accelerometer	$A_x, A_y, A_z$	

TABLE I: On-board sensors. These sensors, along with numerical differentiation, provide the data needed to evaluate all of the terms in (16), (17), and (18).

### IV. ADAPTIVE INPUT AND STATE ESTIMATION

We summarize adaptive input and state estimation [35]–[37] as applied to causal numerical differentiation. Consider the linear discrete-time SISO system

$$x_{k+1} = Ax_k + Bd_k, \quad (19)$$

$$y_k = Cx_k + D_{2,k}v_k, \quad (20)$$

where  $k \geq 0$  is the step,  $x_k \in \mathbb{R}^n$  is the unknown state,  $d_k \in \mathbb{R}$  is unknown input,  $y_k \in \mathbb{R}$  is a measured output,  $v_k \in \mathbb{R}$  is standard white noise, and  $D_{2,k}v_k \in \mathbb{R}$  is the sensor noise at time  $t = kT_s$ , where  $T_s$  is the sample time. The matrices  $A \in \mathbb{R}^{n \times n}$ ,  $B \in \mathbb{R}^{n \times 1}$ , and  $C \in \mathbb{R}^{1 \times n}$ , are assumed to be known and  $D_{2,k}$  is assumed to be unknown.

The sensor-noise covariance is define as  $V_{2,k} \triangleq D_{2,k}D_{2,k}^T$ . The goal of AIE is to estimate  $d_k$  and  $x_k$ .

In the application of AIE to causal numerical differentiation, we use (19) and (20) to model a discrete-time integrator. As a result, AIE furnishes an estimate denoted as  $\hat{d}_k$  for the derivative of the sampled output  $y_k$ . For single discrete-time differentiation, the values are  $A = 1, B = T_s$ , and  $C = 1$ . However, in the case of double discrete-time differentiation,

$$A = \begin{bmatrix} 1 & T_s \\ 0 & 1 \end{bmatrix}, \quad B = \begin{bmatrix} \frac{1}{2}T_s^2 \\ T_s \end{bmatrix}, \quad C = [1 \quad 0]. \quad (21)$$

### A. Input Estimation

AIE comprises three subsystems: the Kalman filter forecast subsystem, the input-estimation subsystem, and the Kalman filter data-assimilation subsystem. First, consider the Kalman filter forecast step

$$x_{fc,k+1} = Ax_{da,k} + B\hat{d}_k, \quad (22)$$

$$y_{fc,k} = Cx_{fc,k}, \quad (23)$$

$$z_k = y_{fc,k} - y_k, \quad (24)$$

where  $x_{da,k} \in \mathbb{R}^n$  is the data-assimilation state,  $x_{fc,k} \in \mathbb{R}^n$  is the forecast state,  $\hat{d}_k$  is the estimate of  $d_k$ ,  $z_k \in \mathbb{R}$  is the residual, and  $x_{fc,0} = 0$ .

Next, in order to obtain  $\hat{d}_k$ , the input-estimation subsystem of order  $n_e$  is given by the exactly proper dynamics

$$\hat{d}_k = \sum_{i=1}^{n_e} P_{i,k} \hat{d}_{k-i} + \sum_{i=0}^{n_e} Q_{i,k} z_{k-i}, \quad (25)$$

where  $P_{i,k} \in \mathbb{R}$  and  $Q_{i,k} \in \mathbb{R}$ . AIE uses recursive least squares (RLS) to minimize  $z_k$  by updating  $P_{i,k}$  and  $Q_{i,k}$  as shown below. The subsystem (25) can be reformulated as

$$\hat{d}_k = \Phi_k \theta_k, \quad (26)$$

where the coefficient vector  $\theta_k$  is defined by

$$\theta_k \triangleq [P_{1,k} \ \cdots \ P_{n_e,k} \ Q_{0,k} \ \cdots \ Q_{n_e,k}]^T \in \mathbb{R}^{l_\theta}, \quad (27)$$

the regressor matrix  $\Phi_k$  is defined by

$$\Phi_k \triangleq [\hat{d}_{k-1} \ \cdots \ \hat{d}_{k-n_e} \ z_k \ \cdots \ z_{k-n_e}] \in \mathbb{R}^{1 \times l_\theta}, \quad (28)$$

and  $l_\theta \triangleq 2n_e + 1$ . (25) can be written using backward shift operator  $\mathbf{q}^{-1}$  as

$$\hat{d}_k = G_{\hat{d}z,k}(\mathbf{q}^{-1})z_k, \quad (29)$$

where

$$G_{\hat{d}z,k} \triangleq D_{\hat{d}z,k}^{-1} N_{\hat{d}z,k}, \quad (30)$$

$$D_{\hat{d}z,k}(\mathbf{q}^{-1}) \triangleq I_{l_d} - P_{1,k} \mathbf{q}^{-1} - \cdots - P_{n_e,k} \mathbf{q}^{-n_e}, \quad (31)$$

$$N_{\hat{d}z,k}(\mathbf{q}^{-1}) \triangleq Q_{0,k} + Q_{1,k} \mathbf{q}^{-1} + \cdots + Q_{n_e,k} \mathbf{q}^{-n_e}. \quad (32)$$

To update the coefficient vector  $\theta_k$ , we define the filtered signals

$$\Phi_{f,k} \triangleq G_{f,k}(\mathbf{q}^{-1})\Phi_k, \quad \hat{d}_{f,k} \triangleq G_{f,k}(\mathbf{q}^{-1})\hat{d}_k, \quad (33)$$

where, for all  $k \geq 0$ ,

$$G_{f,k}(\mathbf{q}^{-1}) = \sum_{i=1}^{n_f} \mathbf{q}^{-i} H_{i,k}, \quad (34)$$

$$H_{i,k} \triangleq \begin{cases} CB, & k \geq i = 1, \\ C\bar{A}_{k-1} \cdots \bar{A}_{k-(i-1)} B, & k \geq i \geq 2, \\ 0, & i > k, \end{cases} \quad (35)$$

and  $\bar{A}_k \triangleq A(I + K_{da,k}C)$ , where  $K_{da,k}$  is the Kalman filter gain given by (41) below. Furthermore, define the *retrospective variable*

$$z_{r,k}(\hat{\theta}) \triangleq z_k - (\hat{d}_{f,k} - \Phi_{f,k}\hat{\theta}), \quad (36)$$

where the coefficient vector  $\hat{\theta} \in \mathbb{R}^{l_\theta}$  denotes a variable for optimization, and define the retrospective cost function

$$\mathcal{J}_k(\hat{\theta}) \triangleq \sum_{i=0}^k [R_z z_{r,i}^2(\hat{\theta}) + R_d (\Phi_i \hat{\theta})^2] + (\hat{\theta} - \theta_0)^T R_\theta (\hat{\theta} - \theta_0), \quad (37)$$

where  $R_z \in (0, \infty)$ ,  $R_d \in (0, \infty)$ , and  $R_\theta \in \mathbb{R}^{l_\theta \times l_\theta}$  is positive definite. Then, for all  $k \geq 0$ , the unique global minimizer  $\theta_{k+1}$  of (37) is given by the RLS update

$$P_{k+1} = P_k - P_k \tilde{\Phi}_k^T \Gamma_k \tilde{\Phi}_k P_k, \quad (38)$$

$$\theta_{k+1} = \theta_k - P_k \tilde{\Phi}_k^T \Gamma_k (\tilde{z}_k + \tilde{\Phi}_k \theta_k), \quad (39)$$

where

$$P_0 \triangleq R_\theta^{-1}, \quad \Gamma_k \triangleq (\tilde{R}^{-1} + \tilde{\Phi}_k P_k \tilde{\Phi}_k^T)^{-1}, \quad \tilde{\Phi}_k \triangleq \begin{bmatrix} \Phi_{f,k} \\ \Phi_k \end{bmatrix},$$

$$\tilde{z}_k \triangleq \begin{bmatrix} z_k - \hat{d}_{f,k} \\ 0 \end{bmatrix}, \quad \tilde{R} \triangleq \begin{bmatrix} R_z & 0 \\ 0 & R_d \end{bmatrix}.$$

Using the updated coefficient vector given by (39), the estimated input at step  $k+1$  is obtained by substituting  $k$  with  $k+1$  in (26). We set  $\theta_0 = 0$ , which results in  $\hat{d}_0 = 0$ . These specific parameters are provided for each example discussed in the paper.

### B. State Estimation

The forecast variable  $x_{fc,k}$  given by (22) is used to obtain the estimate  $x_{da,k}$  of  $x_k$  given by the Kalman filter data-assimilation step

$$x_{da,k} = x_{fc,k} + K_{da,k} z_k, \quad (40)$$

where the Kalman filter gain  $K_{da,k} \in \mathbb{R}^n$ , the data-assimilation error covariance  $P_{da,k} \in \mathbb{R}^{n \times n}$ , and the forecast error covariance  $P_{f,k+1} \in \mathbb{R}^{n \times n}$  are given by

$$K_{da,k} = -P_{f,k} C^T (C P_{f,k} C^T + V_{2,k})^{-1}, \quad (41)$$

$$P_{da,k} = (I_n + K_{da,k} C) P_{f,k}, \quad (42)$$

$$P_{f,k+1} = A P_{da,k} A^T + V_{1,k}, \quad (43)$$

$V_{1,k} \triangleq B \text{var}(d_k - \hat{d}_k) B^T + A \text{cov}(x_k - x_{da,k}, d_k - \hat{d}_k) B^T + B \text{cov}(x_k - x_{da,k}, d_k - \hat{d}_k) A^T$ , and  $P_{f,0} = 0$ .

### C. AIE with Adaptive State Estimation (AIE/ASE)

This section summarizes ASE.  $V_{1,k}$  and  $V_{2,k}$  are unknown in (43) and (41). The goal of ASE is to adapt  $V_{1,k}$  and  $V_{2,k}$ , at each step  $k$ . We define the computable performance metric

$$J_k(V_{1,k-1}, V_{2,k}) \triangleq |\hat{S}_k - S_k|, \quad (44)$$

where  $\hat{S}_k$  is the sample variance of  $z_k$  over  $[0, k]$  given by

$$\hat{S}_k = \frac{1}{k} \sum_{i=0}^k (z_i - \bar{z}_k)^2, \quad \bar{z}_k = \frac{1}{k+1} \sum_{i=0}^k z_i, \quad (45)$$

and  $S_k$  is the variance of the residual  $z_k$  given by the Kalman filter, that is,

$$S_k \triangleq CP_{f,k}C^T + V_{2,k}. \quad (46)$$

Let  $V_{2,\text{adapt},k}$  denote the adapted value of  $V_{2,k}$ . AIE/ASE is thus a specialization of AIE with  $V_{1,k} = V_{1,\text{adapt},k}$  in (43) and  $V_{2,k} = V_{2,\text{adapt},k}$  in (41). In particular,  $V_{1,\text{adapt},k} = \eta I_n$  and  $V_{2,\text{adapt},k} \geq 0$  such that

$$(V_{1,\text{adapt},k}, V_{2,\text{adapt},k}) = \arg \min_{\eta I_n, V_{2,k}} J_k(\eta I_n, V_{2,k}), \quad (47)$$

where  $\eta \in [\eta_L, \eta_U]$  and  $0 \leq \eta_L < \eta \leq \eta_U$ . Defining

$$J_{f,k}(V_{1,k-1}) \triangleq \widehat{S}_k - CP_{f,k}C^T \quad (48)$$

and using (46), (44) can be rewritten as

$$J_k(V_{1,k-1}, V_{2,k}) = |J_{f,k}(V_{1,k-1}) - V_{2,k}|. \quad (49)$$

We construct a set of positive values of  $J_{f,k}$  by enumerating  $V_{1,k-1} = \eta I_n$  as

$$\mathcal{J}_{f,k} \triangleq \{J_{f,k}(\eta I_n) : J_{f,k}(\eta I_n) > 0, \eta_L \leq \eta \leq \eta_U\}. \quad (50)$$

We iterate over  $\eta$  within the range of  $\eta_L$  to  $\eta_U$  with 100 uniform steps.  $V_{1,\text{adapt},k}$  and  $V_{2,\text{adapt},k}$  are then chosen based on following two cases.

**Case 1.** If  $\mathcal{J}_{f,k}$  is not empty, then

$$V_{1,\text{adapt},k} = \arg \min_{\eta I_n} |J_{f,k}(\eta I_n) - \widehat{J}_{f,k}(\alpha)|, \quad (51)$$

$$V_{2,\text{adapt},k} = J_{f,k}(V_{1,\text{adapt},k}), \quad (52)$$

where

$$\widehat{J}_{f,k}(\alpha) \triangleq \alpha \min \mathcal{J}_{f,k} + (1 - \alpha) \max \mathcal{J}_{f,k}, \quad (53)$$

and  $0 \leq \alpha \leq 1$ . For all of the examples in this paper, we set  $\alpha = 1/2$  and omit the argument of  $\widehat{J}_{f,k}$ .

**Case 2.** If  $\mathcal{J}_{f,k}$  is empty, then

$$V_{1,\text{adapt},k} = \arg \min_{\eta I_n} |J_{f,k}(\eta I_n)|, \quad V_{2,\text{adapt},k} = 0. \quad (54)$$

## V. SENSOR FAULT DETECTION

The sensor fault detection method computes each term in (16), (17), and (18) using sensor data and derivatives of sensor data. The equation residuals are then used to detect sensor faults.

We denote the LHS of (16) by  $[L_{s,x,k} \ L_{s,y,k} \ L_{s,z,k}]^T$ , the LHS of (17) by  $[L_{d,x,k} \ L_{d,y,k} \ L_{d,z,k}]^T$ , and the RHS of (16), (17), and (18) by  $[R_{s,x,k} \ R_{s,y,k} \ R_{s,z,k}]^T$ ,  $[R_{d,x,k} \ R_{d,y,k} \ R_{d,z,k}]^T$ , and  $[R_{a,x,k} \ R_{a,y,k} \ R_{a,z,k}]^T$ , respectively. With this notation, we define the error metrics for  $k > \delta$

$$e_{s,q,k} \triangleq \sqrt{\frac{1}{\delta} \sum_{i=k-\delta}^k (L_{s,q,i} - R_{s,q,i})^2}, \quad (55)$$

$$e_{d,q,k} \triangleq \sqrt{\frac{1}{\delta} \sum_{i=k-\delta}^k (L_{d,q,i} - R_{d,q,i})^2}, \quad (56)$$

$$e_{a,q,k} \triangleq \sqrt{\frac{1}{\delta} \sum_{i=k-\delta}^k (L_{d,q,i} - R_{a,q,i})^2}, \quad (57)$$

where  $q$  represents  $x$ ,  $y$ , or  $z$ . Table II summarizes the sensors used to compute the error metrics (55)–(57).

Error Metric	Sensors
$e_{s,q,k}$	Compass, Radar, Rate gyro
$e_{d,q,k}$	Radar, Rate gyro, Accelerometer
$e_{a,q,k}$	Compass, Radar, Accelerometer

TABLE II: Sensors used to compute each error metric, where  $q$  represents  $x$ ,  $y$ , or  $z$ .

## VI. SENSOR FAULT DETECTION FOR GROUND VEHICLES

We focus on ground vehicles that operate on the horizontal plane. We view the radar as a single sensor providing distance data along the body  $x$  and  $y$  directions. Under this assumption, there are five relevant sensors, namely, the compass, the radar, the  $z$  rate gyro, and the  $x$  and  $y$  accelerometer. The relevant error metrics are  $e_{s,x,k}$ ,  $e_{s,y,k}$ ,  $e_{d,x,k}$ ,  $e_{d,y,k}$ ,  $e_{a,x,k}$ , and  $e_{a,y,k}$ .

Each error metric is computed in real time over a trailing data window as the vehicle operates. For each error metric, we specify a cutoff value, namely,  $c_{s,x}$ ,  $c_{s,y}$ ,  $c_{d,x}$ ,  $c_{d,y}$ ,  $c_{a,x}$ , and  $c_{a,y}$  for  $e_{s,x,k}$ ,  $e_{s,y,k}$ ,  $e_{d,x,k}$ ,  $e_{d,y,k}$ ,  $e_{a,x,k}$ , and  $e_{a,y,k}$ , respectively. At each step  $k$ , each error metric is either above cutoff (AC) or below cutoff (BC), and the goal is to use this information to detect faulty sensors. To simplify this procedure, we assume that at most one sensor among the compass, radar,  $z$  rate gyro, and  $x$  and  $y$  accelerometer is faulty at any given time.

Considering all possible values of the error metrics, there are 64 potential scenarios. Assuming that at most one sensor among the compass, radar,  $z$  rate gyro,  $x$  accelerometer, and  $y$  accelerometer is faulty, it follows that, within these 64 cases, only six are feasible. For each of these six cases, Table III specifies the cutoff information that identifies the faulty sensor.

## VII. NUMERICAL EXAMPLES

This section presents numerical examples to demonstrate sensor fault detection. Two types of sensor faults are considered, namely:

- *Bias*: The sensor measurement has a constant offset from the true measurement.
- *Drift*: The sensor measurement has a constant-slope deviation from the true measurement.

In particular, we consider rate-gyro bias and accelerometer drift.

To simulate measurements from a compass, radar,  $z$  rate gyro, and  $x$  and  $y$  accelerometer on a vehicle confined to the horizontal plane, we generate the figure-8 trajectory depicted in Figure 1. The discrete-time equations for this trajectory are  $x(k) = 2 + \sin(2kT_s)$ ,  $y(k) = 2 + \sin(2kT_s) \cos(2kT_s)$ , where the sampling time  $T_s = 0.01$  s/step and  $k \in [1, 6000]$ . To simulate sensor noise, white Gaussian noise is added to

$e_{s,x,k}$	$e_{s,y,k}$	$e_{d,x,k}$	$e_{d,y,k}$	$e_{a,x,k}$	$e_{a,y,k}$	<b>Diagnostic</b>
BC	BC	BC	BC	BC	BC	All sensors are healthy
AC	AC	BC	BC	AC	AC	Compass is faulty
AC	AC	AC	AC	AC	AC	Radar is faulty
BC	AC	AC	AC	BC	BC	$z$ Rate gyro is faulty
BC	BC	AC	BC	AC	BC	$x$ Accelerometer is faulty
BC	BC	BC	AC	BC	AC	$y$ Accelerometer is faulty

TABLE III: Identification of sensor faults for ground vehicles confined to the horizontal plane. At each step, all six error metrics are computed using data obtained during a trailing window. For each metric, BC indicates that the error metric is below cutoff, and AC indicates that the error metric is above cutoff. It is assumed that at most one sensor is faulty; under this assumption, the remaining 58 cases cannot occur.

each sensor measurement, with standard deviations  $\sigma_{r_x} = \sigma_{r_y} = 0.01$  m,  $\sigma_{\omega_z} = 0.001$  rad/s, and  $\sigma_{A_x} = \sigma_{A_y} = 0.1g$ , where  $g = 9.8$  m/s<sup>2</sup>.

In both examples and all cases considered, the transient phase for adaptation of AIE/ASE is less than 250 steps. We thus set  $\delta = 250$  steps. The cutoff values for each error metric are chosen to be twice the error at step  $k = 2\delta$ . This choice ensures that the data used to compute the error metric at step  $k = 2\delta$  lie outside of the transient phase.

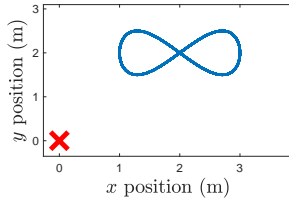


Fig. 1: Position trajectory of the vehicle. The red  $\times$  has zero inertial acceleration and serves as the radar target. The blue curve represents the simulated trajectory.

**Example 7.1: Fault detection for rate-gyro failure.** In this scenario, the rate gyro experiences a failure due to a bias of 1 rad/s starting at 40 s. For single differentiation using AIE/ASE, we set  $n_e = 12$ ,  $n_f = 15$ ,  $R_z = 1$ ,  $R_d = 10^{-4}$ , and  $R_\theta = 10^{-5}I_{25}$ . The parameters  $V_{1,k}$  and  $V_{2,k}$  are adapted, with  $\eta_L = 10^{-6}$  and  $\eta_U = 10^2$  as described in Section IV-C. For double differentiation using AIE/ASE, we set  $n_e = 20$ ,  $n_f = 18$ ,  $R_z = 1$ ,  $R_d = 10^{-7}$ , and  $R_\theta = 10^{-5}I_{41}$ . Similarly,  $V_{1,k}$  and  $V_{2,k}$  are adapted with  $\eta_L = 10^{-6}$  and  $\eta_U = 10^0$  in Section IV-C.

Figure 2 compares  $R_{d,x,k}$  and  $R_{d,y,k}$  with their respective  $L_{d,x,k}$  and  $L_{d,y,k}$ . In Figure 3, the bias introduced at 40 s leads to an abrupt increase in  $e_{d,x,k}$  and  $e_{d,y,k}$  above the cutoff, which indicates that one of the sensors used to compute  $e_{d,x,k}$  and  $e_{d,y,k}$  is faulty. Similarly, Figure 4 and Figure 5 indicates that one of the sensors used to compute  $e_{s,y,k}$  is faulty. Lastly, Figure 6 compares  $R_{a,x,k}$  and  $R_{a,y,k}$  with  $L_{d,x,k}$  and  $L_{d,y,k}$ . Figure 7 shows that  $e_{a,x,k}$  and  $e_{a,y,k}$  are below cutoff. Table III implies that the rate gyro is faulty.

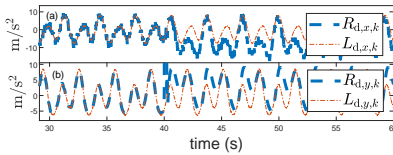


Fig. 2: Example 7.1: Rate gyro with bias. Beginning at 40 s,  $R_{d,x,k}$  in (a) and  $R_{d,y,k}$  in (b) exhibit bias.

**Example 7.2: Fault Detection for Accelerometer failure.** In this scenario, the  $x$ -axis accelerometer experiences a failure due to a drift of 0.05 g/s starting at 40 s. For

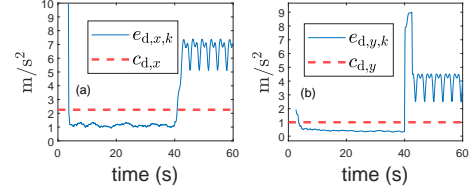


Fig. 3: Example 7.1: Rate gyro with bias.  $e_{d,x,k}$  in (a) and  $e_{d,y,k}$  in (b) abruptly increase above the cutoff values  $c_{d,x}$  and  $c_{d,y}$ , respectively, at 40 s when the bias begins, thus indicating that one of the sensors used to compute  $e_{d,x,k}$  and  $e_{d,y,k}$  is faulty.

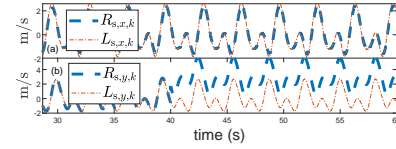


Fig. 4: Example 7.1: Rate gyro with bias. (a)  $R_{s,x,k}$  follows  $L_{s,x,k}$ . (b) Beginning at 40 s,  $R_{s,y,k}$  exhibits bias.

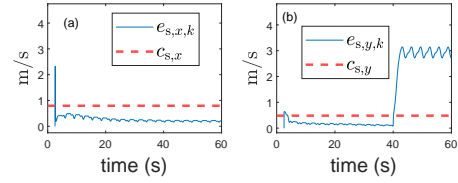


Fig. 5: Example 7.1: Rate gyro with bias. (a)  $e_{s,x,k}$  remain below cutoff  $c_{s,x}$ . (b)  $e_{s,y,k}$  abruptly increases above  $c_{s,y}$  at 40 s when the bias begins, thus indicating that one of the sensors used to compute  $e_{s,y,k}$  is faulty.

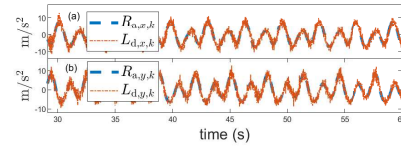


Fig. 6: Example 7.1: Rate gyro with bias. (a)  $R_{a,x,k}$  follows  $L_{d,x,k}$ . (b)  $R_{a,y,k}$  follows  $L_{d,y,k}$ , thus indicating no bias.

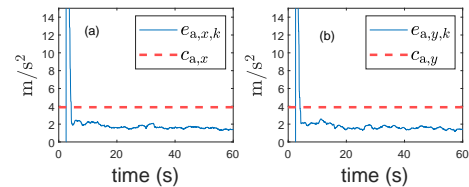


Fig. 7: Example 7.1: Rate gyro with bias. In (a) and (b), both  $e_{a,x,k}$  and  $e_{a,y,k}$  remain below cutoff, indicating no sensor faults in computing error metric  $e_{a,q,k}$ .

both single and double differentiation using AIE/ASE, the parameters remain the same as those used in Example 7.1.

Figure 8 compares  $R_{d,x,k}$  and  $R_{d,y,k}$  with their respective  $L_{d,x,k}$  and  $L_{d,y,k}$ . In Figure 9, the drift begins at 40 s and leads to an abrupt increase in  $e_{d,x,k}$  above  $c_{d,x}$ , which indicates that one of the sensors used to compute  $e_{d,x,k}$  is faulty. Figure 10 compares  $R_{s,x,k}$  and  $R_{s,y,k}$  with  $L_{s,x,k}$  and

$L_{s,y,k}$ . Figure 11 shows that  $e_{s,x,k}$  and  $e_{s,y,k}$  are below the cutoff. Similarly, Figure 12 and Figure 13 indicates that one of the sensors used to compute  $e_{a,x,k}$  is faulty. Table III implies that the accelerometer is faulty.

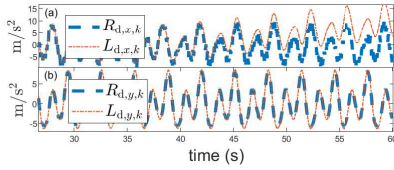


Fig. 8: Example 7.2: Accelerometer with drift. (a) Beginning at 40 s,  $L_{d,x,k}$  exhibits drift. (b)  $R_{d,y,k}$  follows  $L_{d,y,k}$ .

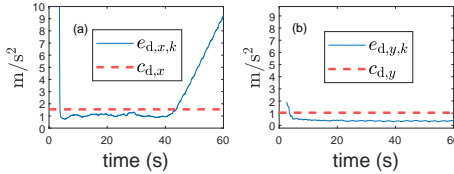


Fig. 9: Example 7.2: Accelerometer with drift.  $e_{d,x,k}$  in (a) abruptly increases at 40 s when the drift begins, hence indicate a fault in the sensors used to compute  $e_{d,q,k}$ . (b)  $e_{d,y,k}$  remains below the cutoff.

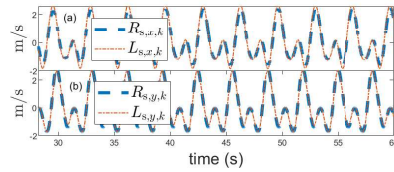


Fig. 10: Example 7.2: Accelerometer with drift. (a)  $R_{s,x,k}$  follows  $L_{s,x,k}$ . (b)  $R_{s,y,k}$  follows  $L_{s,y,k}$ , thus indicating no drift.

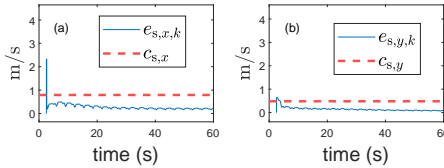


Fig. 11: Example 7.2: Accelerometer with drift. In (a) and (b), both  $e_{s,x,k}$  and  $e_{s,y,k}$  decrease, indicating no sensor fault in computing error metric  $e_{s,q,k}$ .

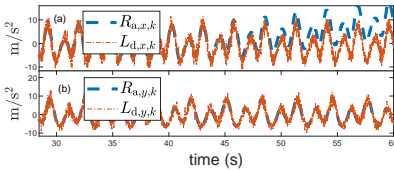


Fig. 12: Example 7.2: Accelerometer with drift. Beginning at 40 s,  $R_{a,x,k}$  in (a) exhibits drift. (b)  $R_{a,y,k}$  follows  $L_{d,y,k}$ .

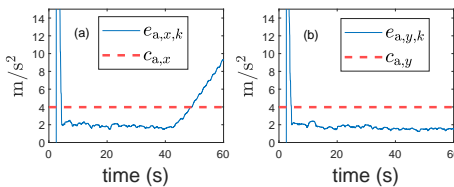


Fig. 13: Example 7.2: Accelerometer with drift.  $e_{a,x,k}$  in (a) abruptly increases at 40 s when the drift begins, hence indicate a fault in the sensors used to compute  $e_{a,x,k}$ . (b)  $e_{a,y,k}$  remains below cutoff.

## VIII. CONCLUSIONS

This paper introduced a kinematics-based approach for detecting and identifying sensor faults in autonomous vehicles. This method utilizes data from radar, rate gyro, compass, and accelerometer sensors, along with their corresponding single and double derivatives computed by using the adaptive input and state estimation algorithm (AIE/ASE). Six error metrics were used to detect and identify faulty sensors. Numerical examples demonstrated the application of this technique for identifying faults in the rate gyro and  $x$ -axis accelerometer. In future research, the methodology will be extended to sensor fault detection in aerial vehicles.

## ACKNOWLEDGMENTS

This research was supported by NSF grant CMMI 2031333.

## REFERENCES

- [1] D. Li, Y. Wang, J. Wang, C. Wang, and Y. Duan, "Recent Advances in Sensor Fault Diagnosis: A Review," *Sensors and Actuators A: Physical*, vol. 309, p. 111990, 2020.
- [2] R. J. Patton, "Fault detection and diagnosis in aerospace systems using analytical redundancy," in *IEE Colloquium on Condition Monitoring and Fault Tolerance*, pp. 1–1, IET, 1990.
- [3] I. Samy, I. Postlethwaite, and D.-W. Gu, "Survey and application of sensor fault detection and isolation schemes," *Control Engineering Practice*, 2011. doi: 10.1016/j.conengprac.2011.03.002.
- [4] I. Hwang, S. Kim, Y. Kim, and C. E. Seah, "A survey of fault detection, isolation, and reconfiguration methods," *IEEE Trans. Contr. Sys. Tech.*, vol. 18, no. 3, pp. 636–653, 2010.
- [5] R. Doraiswami, M. Stevenson, and C. Diduch, *Identification of Physical Systems: Applications to Condition Monitoring, Fault Diagnosis, Soft Sensor, and Controller Design*. Wiley, 2014.
- [6] R. Isermann, "Process fault detection based on modeling and estimation methods—a survey," *Automatica*, vol. 20, no. 4, pp. 387–404, 1984.
- [7] R. Isermann, *Fault-Diagnosis Systems*. Springer, 2006.
- [8] R. Isermann, *Fault-Diagnosis Applications: Model-Based Condition Monitoring: Actuators, Drives, Machinery, Plants, Sensors, and Fault-tolerant Systems*. Springer, 2011.
- [9] J. J. Gertler, *Fault Detection and Diagnosis in Engineering Systems*. New York, NY: Marcel Dekker Inc., 1998.
- [10] V. Venkatasubramanian, R. Rengaswamy, K. Yin, and S. N. Kavuri, "A review of process fault detection and diagnosis part i: Quantitative model-based methods," *Computers and Chemical Engineering*, vol. 27, pp. 293–311, 2003.
- [11] R. Isermann, "Supervision, fault-detection and fault-diagnosis methods - an introduction," *Control Engineering Practice*, vol. 5, no. 5, pp. 639–652, 1997.
- [12] R. J. Patton and J. Chen, "Observer-based fault detection and isolation: robustness and applications," *Control Engineering Practice*, vol. 5, no. 5, pp. 671–682, 1997.
- [13] S. X. Ding, *Model-Based Fault Diagnosis Techniques: Design Schemes, Algorithms, and Tools*. Berlin-Heidelberg, DE: Springer-Verlag, 2008.
- [14] L. H. Chiang, E. L. Russell, and R. D. Braatz, *Fault Detection and Diagnosis in Industrial Systems*. London, UK: Springer-Verlag, 2001.
- [15] P. M. Frank and X. Ding, "Survey of robust residual generation and evaluation methods in observer-based fault detection systems," *Journal of Process Control*, vol. 7, no. 6, pp. 403–424, 1997.
- [16] R. Rengaswamy and V. Venkatasubramanian, "A fast training neural network and its updation for incipient fault detection and diagnosis," *Computers and Chemical Engineering*, vol. 24, no. 2–7, pp. 431–437, 2000.
- [17] R. J. Patton, P. M. Frank, and R. N. Clark, *Issues of Fault Diagnosis for Dynamic Systems*. London, UK: Springer-Verlag, 2000.
- [18] R. Rajamani and A. Ganguli, "Sensor fault diagnostics for a class of non-linear systems using linear matrix inequalities," *Int. J. Contr.*, vol. 77, no. 10, pp. 920–930, 2004.

- [19] P. M. Frank, "Fault diagnosis in dynamic systems using analytical and knowledge-based redundancy: A survey and some new results," *Automatica*, vol. 26, no. 3, pp. 459–474, 1990.
- [20] E. Chow and A. S. Willsky, "Analytical redundancy and the design of robust failure detection systems," *IEEE Trans. Autom. Contr.*, vol. 29, no. 7, pp. 603–614, 1984.
- [21] M. Staroswiecki and G. Comtet-Varga, "Analytical redundancy relations for fault detection and isolation in algebraic dynamic systems," *Automatica*, vol. 37, no. 5, pp. 687–699, 2001.
- [22] J. Chen and R. J. Patton, *Robust Model-Based Fault Diagnosis for Dynamic Systems*. Springer, 2012.
- [23] X. Zhang, T. Parisini, and M. M. Polycarpou, "Sensor bias fault isolation in a class of nonlinear systems," *IEEE Trans. Autom. Contr.*, vol. 50, no. 3, pp. 370–376, 2005.
- [24] P. Freeman, P. Seiler, and G. J. Balas, "Air data system fault modeling and detection," *Contr. Eng. Practice*, vol. 21, pp. 1290–1301, 2013.
- [25] K. F. Martin, "A review by discussion of condition monitoring and fault diagnosis in machine tools," *International Journal of Machine Tools and Manufacture*, vol. 34, no. 4, pp. 527–551, 1994.
- [26] R. Kothamasu, S. H. Huang, and W. H. VerDuin, "System health monitoring and prognostics - a review of current paradigms and practices," *International Journal of Advanced Manufacturing Technology*, vol. 28, pp. 1012–1024, 2006.
- [27] R. Yan and R. X. Gao, "Approximate entropy as a diagnostic tool for machine health monitoring," *Mechanical Systems and Signal Processing*, vol. 21, no. 2, pp. 824–839, 2007.
- [28] O. Basir and X. Yuan, "Engine fault diagnosis based on multi-sensor information fusion using Dempster-Shafer evidence theory," *Information Fusion*, vol. 8, no. 4, pp. 379–386, 2007.
- [29] M. Basseville, "Detecting changes in signals and systems - a survey," *Automatica*, vol. 24, no. 3, pp. 309–326, 1988.
- [30] M. Basseville, "On-board component fault detection and isolation using the statistical local approach," *Automatica*, vol. 34, no. 11, pp. 1391–1416, 1998.
- [31] M. Basseville and I. V. Nikiforov, *Detection of Abrupt Changes - Theory and Application*. Englewood Cliffs, NJ, USA: Prentice-Hall, 1993.
- [32] S. Gururajan, M. Fravolini, M. Rhudy, A. Moschitta, and M. Napolitano, "Evaluation of sensor failure detection, identification and accommodation (SFDIA) performance following common-mode failures of pitot tubes," *SAE Technical Paper*, Sept 2014.
- [33] M. L. Fravolini, M. Rhudy, S. Gururajan, S. Cascianelli, and M. Napolitano, "Experimental evaluation of two pitot free analytical redundancy techniques for the estimation of the airspeed of an uav," *SAE International Journal of Aerospace*, vol. 7, no. 2014-01-2163, pp. 109–116, 2014.
- [34] R. C. Swischuk and D. L. Allaire, "A machine learning approach to aircraft sensor error detection and correction," in *2018 AIAA/ASCE/AHS/ASC Structures, Structural Dynamics, and Materials Conference*, p. 1164, 2018.
- [35] S. Verma, S. Sanjeevini, E. D. Sumer, A. Girard, and D. S. Bernstein, "On the Accuracy of Numerical Differentiation Using High-Gain Observers and Adaptive Input Estimation," in *Proc. Amer. Contr. Conf.*, pp. 4068–4073, 2022.
- [36] S. Verma, S. Sanjeevini, E. D. Sumer, and D. S. Bernstein, "Real-time numerical differentiation of sampled data using adaptive input and state estimation," arXiv:2308.08074, 2023.
- [37] A. Ansari and D. S. Bernstein, "Input estimation for nonminimum-phase systems with application to acceleration estimation for a maneuvering vehicle," *IEEE Trans. Autom. Contr. Sys. Tech.*, vol. 27, no. 4, pp. 1596–1607, 2019.